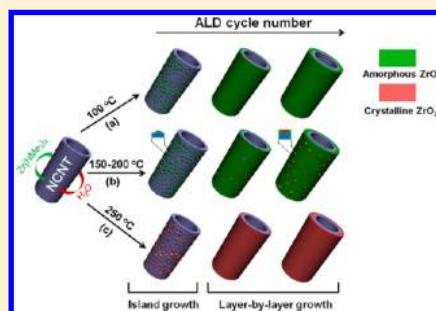


Crystallinity-Controlled Synthesis of Zirconium Oxide Thin Films on Nitrogen-Doped Carbon Nanotubes by Atomic Layer Deposition

Jian Liu,[†] Xiangbo Meng,[‡] Mohammad Norouzi Banis,[†] Mei Cai,[§] Ruying Li,[†] and Xueliang Sun^{*,†}[†]Department of Mechanical and Materials Engineering, University of Western Ontario, London, Ontario, Canada N6A 5B9[‡]Chemistry Department, Brookhaven National Laboratory, Upton, New York 11973, United States[§]General Motors R&D Center, Warren, Michigan 48090-9055, United States

Supporting Information

ABSTRACT: Zirconium oxide (ZrO_2) thin film was deposited on nitrogen-doped carbon nanotubes (NCNTs) by atomic layer deposition (ALD) using tetrakis(dimethylamido)zirconium(IV) and water as precursors. The observation using scanning electron microscope and transmission electron microscope (TEM) revealed that the tubular films of 100-cycle ZrO_2 were very uniform and conformal on NCNTs. Further characterization using X-ray diffraction, Raman spectroscopy, selected area electron diffraction, and high-resolution TEM disclosed that the crystallinity of the deposited ZrO_2 films was controllable with deposition temperatures in the range of 100–250 °C. In contrast to the pure amorphous ZrO_2 film deposited at 100 °C, tetragonal crystalline ZrO_2 film was prepared at 250 °C, while a mixture of the former two phases was found between 150 and 200 °C. In all cases, the growth of ZrO_2 tubular films on NCNTs showed a transformation from an island-growth mode to a layer-by-layer growth mode with increasing ALD cycles. The ZrO_2 -NCNT nanocomposites with controllable crystallinity will have great potential for various applications in fuel cells, batteries, electronics devices, and chemical sensors.



1. INTRODUCTION

Since the work by Iijima in 1991,¹ carbon nanotubes (CNTs) have been drawing much attention from various areas because of their unique properties.^{2,3} Up to now, CNTs have been involved in a wide range of potential applications, such as reinforced materials, nanoelectronic devices, field emission display sources, and energy storage and conversion devices.^{4,5} Recently, great interest has been raised to make one-dimensional nanocomposites by using CNTs as supports for the deposition of various materials.^{6–9} In particular, CNTs have been considered as the most promising templates for fabricating metal oxide–CNT nanocomposites, which possess exceptional chemical, mechanical, and physical properties.^{10–15} These advanced nanocomposites are likely to become key components in the next generation of magnetic, optical, and electronic devices.

Zirconium oxide (ZrO_2) is an attractive material in many fields because of its excellent mechanical, thermal, optical, and electrical characteristics.^{16,17} ZrO_2 can present three polymorphic crystalline structures, that is, monoclinic (below 1170 °C), tetragonal (1170–2370 °C), and cubic (above 2370 °C).¹⁷ Recently, there were many efforts devoted to fabricate ZrO_2 -CNT nanocomposites in hopes of broadening the applications of ZrO_2 .^{18–23} For example, ZrO_2 -CNT nanocomposite prepared by a hydrothermal method was found to be a good biocompatible matrix for protein immobilization.¹⁸ In addition, it was also found that the Pt catalyst supported by ZrO_2 -CNT nanocomposites exhibited significantly improved catalytic activity toward methanol and ethanol oxidation in direct

methanol and ethanol fuel cells compared with that supported by either CNTs or commercial C.^{19,20} Moreover, CNT transistors integrated with high-k ZrO_2 were applied as advanced gate dielectrics, which will be crucial for future molecular electronics.²¹ Thus, ZrO_2 -CNT nanocomposites are promising for applications in fuel cells, batteries, electronics devices, and chemical sensors.

To fulfill these applications, it is of great importance to controllably synthesize ZrO_2 -CNT nanocomposites. In previous studies, the fabrication of ZrO_2 -CNT nanocomposites was mainly achieved by solution-based methods.^{16,17,23–25} For example, Sun et al.²³ synthesized ZrO_2 -CNT nanocomposites via decomposition of $\text{Zr}(\text{NO}_3)_4 \cdot 8\text{H}_2\text{O}$ in supercritical carbon dioxide–ethanol solution with dispersed CNTs at relatively low temperatures. Shan and Gao²⁴ prepared ZrO_2 -CNT nanocomposites with phase-controlled ZrO_2 by hydrothermal treatment of CNTs in $\text{ZrOCl}_2 \cdot 8\text{H}_2\text{O}$ aqueous solution at 150 °C. Most of these studies were focused on controlling the phase^{17,24,25} or morphology¹⁶ of ZrO_2 coated on CNTs, and the CNTs used in these studies required a pretreatment process by either covalent²⁶ or noncovalent^{14,27} methods to functionalize their inert surface. The pretreatment might adversely affect the inherent properties of the CNTs.

Herein, we developed an alternative approach to synthesize ZrO_2 -CNT nanocomposites. This approach features crystal-

Received: March 25, 2012

Revised: May 18, 2012

Published: June 4, 2012

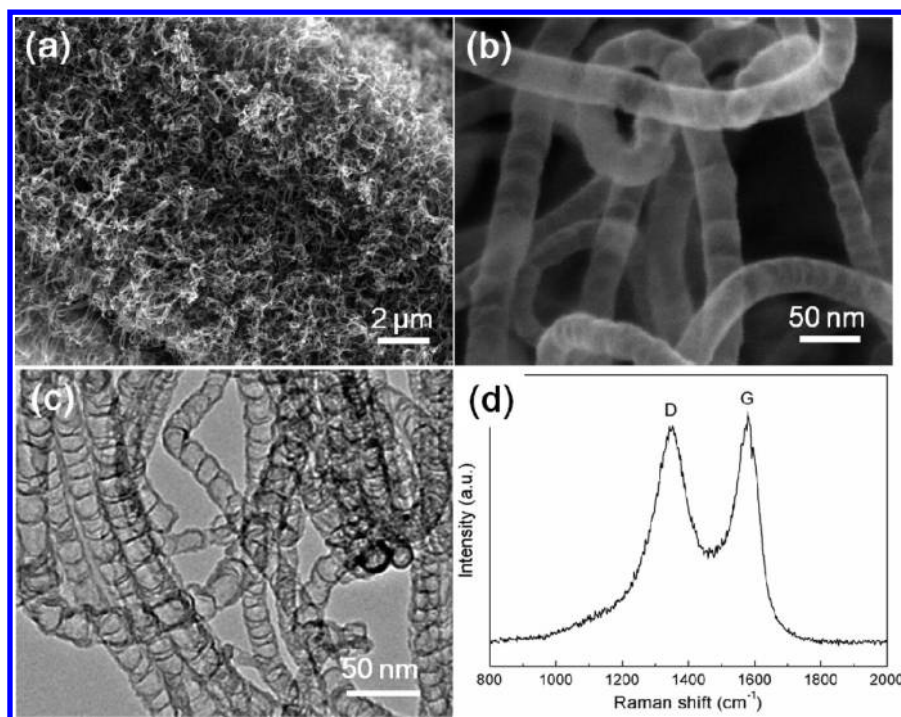
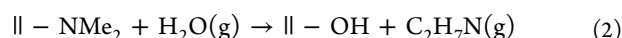
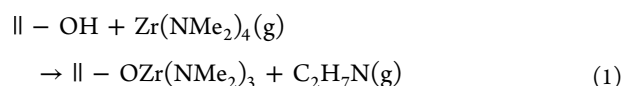


Figure 1. (a, b) SEM images, (c) TEM image, and (d) Raman spectrum of NCNTs synthesized by the CVD method.

linity-controlled deposition of ZrO_2 tubular films directly on nitrogen-doped carbon nanotubes (NCNTs) using atomic layer deposition (ALD), which has been our research interest both in synthesizing^{28–32} and in applications.^{33,34} ALD is a unique technique which allows the deposition of conformal and uniform thin films via sequential and self-terminating gas–solid reactions with controlled film thickness at atomic level.^{35,36} The coating of ZrO_2 on CNTs was previously achieved with the use of ZrCl_4 and H_2O as precursors, whereas detailed studies are still lacking.²¹ Moreover, the use of ZrCl_4 as Zr precursor may constrain the application of ZrO_2 because ZrCl_4 suffers from serious processing problems including the corrosion of deposition system caused by HCl generated during the reaction, high risk of small particles being transported into substrates, and high evaporation temperature (165 °C) because of its low volatility.³⁷ In comparison, tetrakis(dimethylamido)-zirconium(IV) [$\text{Zr}(\text{NMe}_2)_4$] as an ALD precursor has several advantages over ZrCl_4 , such as sufficient volatility, thermal stability, and high reactivity to a hydroxylated surface.^{38–40} Using $\text{Zr}(\text{NMe}_2)_4$ and H_2O as ALD precursors, for example, ZrO_2 films were successfully deposited on Si and glassy carbon substrates with a growth per cycle (GPC) of 0.096 ± 0.002 nm in the range of 50–250 °C.^{38,39} It was reported that the ALD of ZrO_2 (ALD- ZrO_2) using these two precursors consists of two half reactions³⁸



where \parallel represents substrate surface and (g) denotes vapor species. Therefore, in this work, $\text{Zr}(\text{NMe}_2)_4$ and H_2O were employed as precursors for ALD- ZrO_2 . The NCNTs were homemade and were suitable for ALD processes without any additional pretreatment steps.^{29,31} In summary, this work

describes the uniform deposition of ALD- ZrO_2 films on NCNTs with not only precisely controlled thickness at nanoscale level but also highly tunable crystallinity from amorphous to crystalline. In addition, the growth process of ALD- ZrO_2 on NCNTs was explored, and the growth mechanisms of ALD- ZrO_2 on NCNTs were proposed. This kind of ZrO_2 –NCNT nanocomposites synthesized by ALD may find many potential applications, such as fuel cells, batteries, electronics, and gas sensors.

2. EXPERIMENTAL SECTION

2.1. Synthesis of NCNTs. NCNTs were prepared by a chemical vapor deposition (CVD) method using melamine ($\text{C}_3\text{H}_6\text{N}_6$, 99+%, Aldrich) as the only source for both carbon and nitrogen. The substrate used for the growth of NCNTs was a carbon paper, which had been sequentially coated by an aluminum film (30 nm in thickness) and an iron film (5 nm in thickness) in a sputtering system. The aluminum film as a buffer layer could improve the quality and growth rate of NCNTs, while the iron film could catalyze the growth of NCNTs.⁴¹ In a typical process, NCNTs were grown by the pyrolysis of melamine at 800 °C using argon (99.999% in purity) as a protective and carrier gas. More details can be found in our previous work.⁴²

2.2. ZrO_2 –NCNTs by ALD. The deposition of ZrO_2 on NCNTs was achieved by alternatively supplying $\text{Zr}(\text{NMe}_2)_4$ (99%, STREM) and deionized water (H_2O) into a commercial ALD reactor (Savannah 100, Cambridge Nanotech Inc., United States). $\text{Zr}(\text{NMe}_2)_4$ was heated to 75 °C, while water was kept at room temperature. In that case, sufficient precursor vapors could be supplied for the deposition of ZrO_2 . Additionally, the delivery lines were heated to 100 °C to prevent the precursors from condensation. Nitrogen gas (99.999% in purity) was used as a carrier gas with a flow rate of 20 sccm, and the ALD reactor was maintained at a low level of base pressure (typically 0.3–0.4 Torr) by a vacuum pump (Pascal 2005 I, Adixen). One

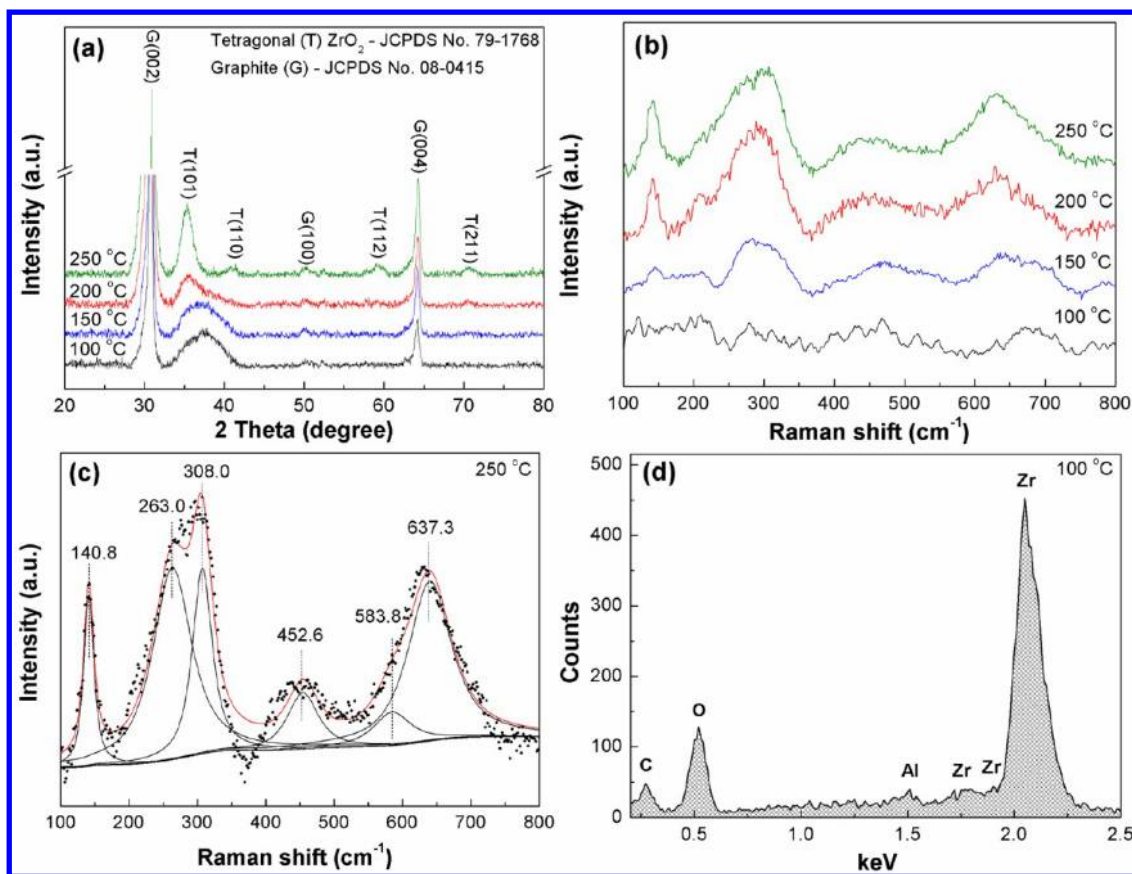


Figure 2. XRD patterns (a) and Raman spectra (b) of 100-cycle ZrO_2 -NCNTs prepared at 250, 200, 150, and 100 °C. (c) Deconvolution of Raman spectrum of 100-cycle ZrO_2 -NCNTs prepared at 250 °C. (d) EDS spectrum of 100-cycle ZrO_2 -NCNTs prepared at 100 °C.

ALD cycle was executed with the following six steps: (1) a supply of $\text{Zr}(\text{NMe}_2)_4$ with a t_1 pulse time; (2) a 3.0 s extended exposure of $\text{Zr}(\text{NMe}_2)_4$ to NCNTs; (3) a purging of oversupplied $\text{Zr}(\text{NMe}_2)_4$ and any byproducts with a t_2 purge time; (4) a supply of H_2O with a t_3 pulse time; (5) a 3.0 s extended exposure of H_2O to NCNTs; (6) a purging of excess H_2O and any byproducts with a t_4 purge time. In short, the deposition procedure can be described as t_1 - t_2 - t_3 - t_4 . ZrO_2 was deposited on NCNTs by repeating the above ALD cycle at 250, 200, 150, and 100 °C, respectively.

2.3. Characterization of ZrO_2 -NCNTs. The morphology and structure of as-synthesized ZrO_2 -NCNT nanocomposites were characterized by a field-emission scanning electron microscope (SEM, Hitachi S4800) equipped with energy-dispersive X-ray spectroscopy (EDS), transmission electron microscope (TEM, Hitachi H-7000), high-resolution TEM (HRTEM, JEOL 2010 FEG), micro-X-ray diffraction (XRD, Bruker D8, $\text{Co K}\alpha$ source, $\lambda = 1.7892 \text{ \AA}$), and Raman spectrometer (HORIBA Scientific LabRAW HR800) with an incident laser beam of 532.4 nm.

3. RESULTS AND DISCUSSION

3.1. Results. Figure 1 (a–c) shows the morphology and structure of NCNTs prepared by the CVD method. From Figure 1 (a, b), it can be seen that the carbon paper was totally covered by high-density NCNTs with diameters in a range of 20–35 nm. The TEM image in Figure 1c indicates that the synthesized NCNTs possess a typical bamboolike structure, which is induced by nitrogen doping in the hexagonal framework of carbon layers.^{42,43} The Raman spectrum of the

NCNTs shows two first-order Raman peaks centered at $\sim 1342 \text{ cm}^{-1}$ and $\sim 1582 \text{ cm}^{-1}$, which are so-called D-band and G-band, respectively, as seen in Figure 1 d. The intensity ratio between D-band and G-band (I_D/I_G) is calculated to be 0.94 for the NCNTs revealing its high degree of disorder because of nitrogen doping.⁴³

To find out the conditions for saturated growth of ALD- ZrO_2 , the pulse time and purge time for both precursors were optimized. The deposition temperature was chosen to be 200 °C using $\text{Zr}(\text{NMe}_2)_4$ and H_2O as precursors.³⁸ The optimization was carried out by changing one parameter at a time while keeping the others constant. The results indicated that a 0.5 s pulse of $\text{Zr}(\text{NMe}_2)_4$ and a 1.0 s pulse of H_2O are sufficient to realize saturated growth of ALD- ZrO_2 thin film on NCNTs (Figure SI-1 of the Supporting Information). The purge time required is at least 30 s in order to avoid CVD-like growth of ZrO_2 (Figure SI-2a, b of the Supporting Information) and to achieve uniform deposition of ALD- ZrO_2 thin film (Figure SI-2c, d of the Supporting Information). A prolonged purge time had no obvious effect on the thickness and uniformity of ALD- ZrO_2 thin film (Figure SI-2e, f of the Supporting Information). Therefore, all the ALD- ZrO_2 was conducted with the procedure of 0.5 s, 30 s, 1 s, 30 s.

3.1.1. Crystalline Development of ALD- ZrO_2 . The structural phases of 100-cycle ALD- ZrO_2 prepared at 250, 200, 150, and 100 °C were identified by XRD and Raman techniques, and the results are presented in Figure 2. Figure 2a shows the XRD patterns of 100-cycle ZrO_2 -NCNTs prepared at 250, 200, 150, and 100 °C. It can be seen that all samples exhibit two strong peaks at 30° and 64° and a weak one at 50°, which are indexed

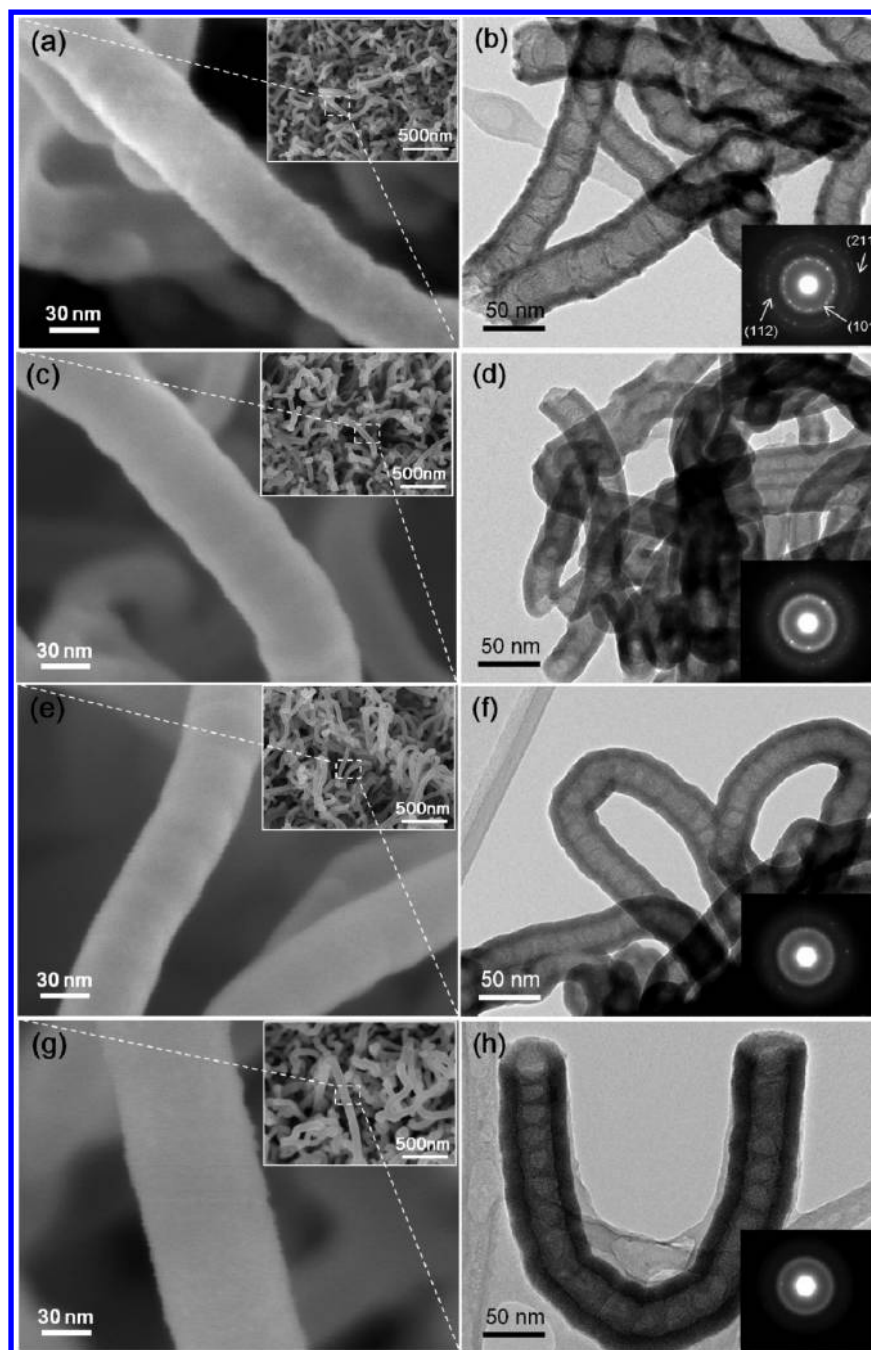


Figure 3. SEM (a, c, e, g) and TEM (b, d, f, h) images of 100-cycle ZrO_2 -NCNTs prepared at 250 °C (a, b), 200 °C (c, d), 150 °C (e, f), and 100 °C (g, h). (Inset in each TEM image corresponds to its SAED pattern.)

as (002), (004), and (100) planes of graphite (JCPDS PDF No. 08-0415), respectively. They are apparently induced by the carbon paper and NCNTs grown on it. For the ZrO_2 -NCNTs prepared at 250 °C, the other peaks located at 36°, 41°, 59°, and 71° are well consistent with the planes of (101), (110), (112), and (211) of tetragonal ZrO_2 (JCPDS PDF No. 79-1768), respectively. The four peaks could be also assigned to cubic ZrO_2 , however, the existence of which is excluded later by Raman examination. With a decrease in deposition temperature, the peak of (101) plane of tetragonal ZrO_2 shifts to higher degrees and becomes broader in terms of half-width. In the meantime, the other peaks belonging to tetragonal ZrO_2 become weaker in intensity. They totally disappear in the ZrO_2 -NCNTs prepared at 100 °C. The XRD results indicate

that the ALD- ZrO_2 experienced a gradual decrease in its crystallinity when decreasing the deposition temperature. Raman spectroscopy was carried out on the above samples in a region of 100–800 cm^{-1} , and the results are presented in Figure 2b, c. From Figure 2b, it can be seen that Raman spectra are approximately the same for ZrO_2 -NCNTs prepared at 250, 200, and 150 °C. Deconvolution of the Raman spectrum for ZrO_2 -NCNTs prepared at 250 °C reveals six peaks located at 140.8, 263.0, 308.0, 452.6, 538.8, and 637.3 cm^{-1} (Figure 2c), which can be clearly assigned to the six Raman active modes ($A_{1g} + 2B_{1g} + 3E_g$) of tetragonal ZrO_2 .^{44,45} Similar results were also obtained for ZrO_2 -NCNTs prepared at 200 and 150 °C. For the ZrO_2 -NCNTs prepared at 100 °C, however, broad peaks with weak intensities are observed in their Raman

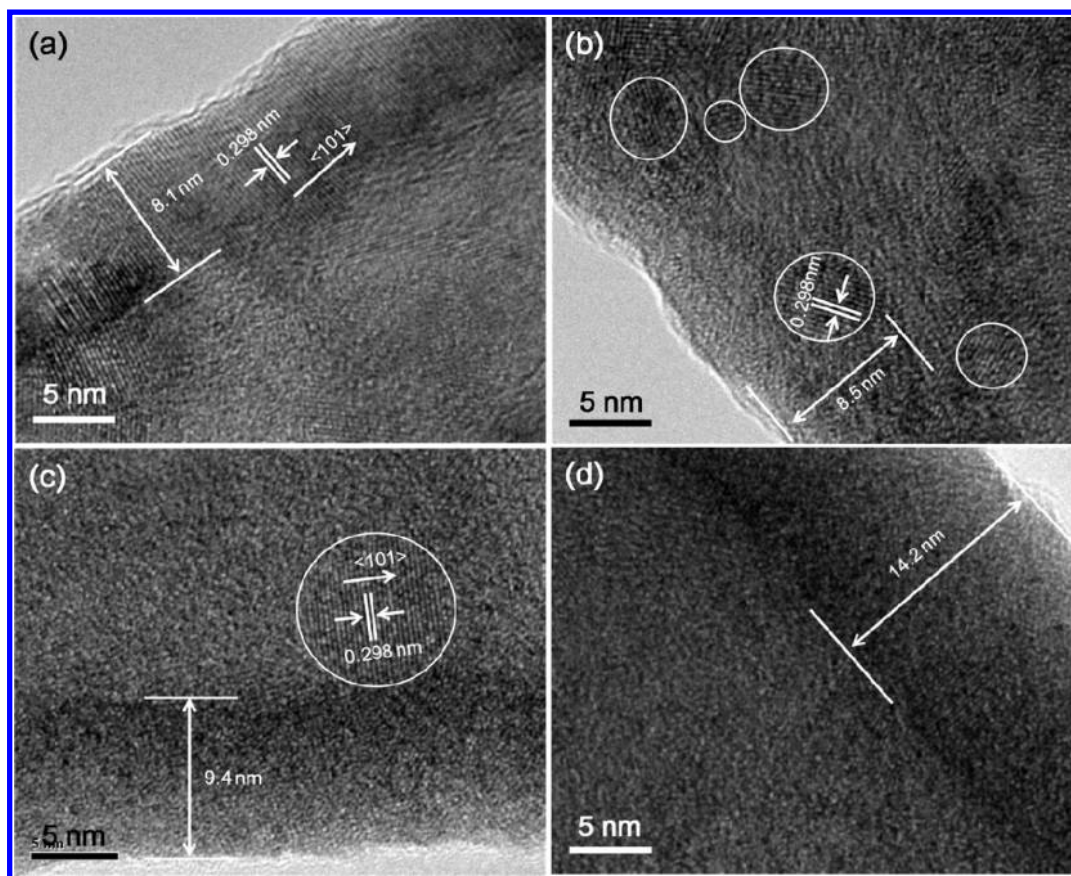


Figure 4. HRTEM images of 100-cycle ZrO_2 -NCNTs prepared at (a) 250 °C, (b) 200 °C, (c) 150 °C, and (d) 100 °C.

spectrum (Figure 2b) from which it is hard to identify the phase of the deposited ZrO_2 . This kind of Raman spectrum is probably due to the extremely limited long-range periodicity of ZrO_2 prepared at such low temperature.⁴⁵ Nonetheless, EDS analysis verified the presence of Zr and O elements in the ZrO_2 -NCNTs prepared at 100 °C as seen in Figure 2d.

Tetragonal ZrO_2 is generally stable at high temperatures (1170–2370 °C),¹⁷ while in our case, it was not only prepared at temperatures below 250 °C but was also stable at room temperature. The occurrence of tetragonal ZrO_2 at low temperatures has been reported previously.^{46–49} Earlier studies believed that the low-temperature tetragonal ZrO_2 should be ascribed to grain size effect, that is, ZrO_2 with small size and high surface area can provide high surface energy to stabilize metastable tetragonal ZrO_2 at low temperatures.^{48,49} In this work, NCNTs acted as promising ALD- ZrO_2 substrate with high surface area and high surface energy, which in return help the stabilization of tetragonal ZrO_2 at temperatures below 250 °C.

The morphologies of 100-cycle ALD- ZrO_2 on NCNTs prepared at 250, 200, 150, and 100 °C were observed by SEM and TEM, and the results are presented in Figure 3. From Figure 3 (a, c, e, g), it can be clearly seen that NCNTs are homogeneously coated with ZrO_2 tubular thin films at deposition temperatures of 250, 200, 150, and 100 °C. TEM observation reveals that these ZrO_2 thin films are extremely uniform and conformal on NCNTs in all the cases as shown in Figure 3 (b, d, f, h). Furthermore, selected area electron diffraction (SAED) was employed and the crystallinity of ALD- ZrO_2 was revealed as shown by the insets in Figure 3 (b, d, f, h). For the ZrO_2 -NCNTs prepared at 250 °C, the SAED

diffraction rings can be indexed as (101), (112), and (211) planes of tetragonal ZrO_2 indicating its polycrystalline feature (see the inset in Figure 3b). From Figure 3d and f, it can be clearly seen that the diffraction rings become more diffusive with the decreasing deposition temperature. In the case of 100 °C, only diffusive rings are observed as shown by the inset in Figure 3h manifesting that the ALD- ZrO_2 consists of only the amorphous phase. The SAED results indicate that ALD- ZrO_2 on NCNTs is temperature-dependent in the crystallinity. In particular, the information extracted from SAED and XRD results (see Figure 2a) is consistent with the crystallinity of the ALD- ZrO_2 prepared at different deposition temperatures.

The microstructures of 100-cycle ALD- ZrO_2 were further investigated using HRTEM as shown in Figure 4. Figure 4a reveals that ALD- ZrO_2 thin film is fully crystalline at 250 °C, and the interplanar spacing of 0.298 nm (as marked in Figure 4a) is consistent with the spacing distance between (101) planes of tetragonal ZrO_2 . In the case of 200 °C, the ZrO_2 thin film is composed of both crystalline nanoparticles and amorphous layers. These nanoparticles with tetragonal ZrO_2 phase randomly distribute in the matrix of the amorphous ZrO_2 as shown in Figure 4b. At the lower deposition temperature of 150 °C as shown in Figure 4c, it is found that these nanoparticles become sparse, and the matrix of amorphous ZrO_2 layers takes the dominance. At the lowest deposition temperature of 100 °C as shown in Figure 4d, only amorphous ZrO_2 thin film can be identified. On the basis of the above results, it can be concluded that the crystallinity of ALD- ZrO_2 is temperature-dependent, that is, the deposited ZrO_2 shows crystalline tetragonal phase at 250 °C, amorphous phase at 100

°C, and a mixture of the former two in the range of 200–150 °C.

During ALD processes, growth per cycle (GPC) is an important measure to evaluate the growth ability of desirable materials. In this work, the GPC of ALD-ZrO₂ is calculated on the basis of the thickness of 100-cycle ALD-ZrO₂ thin films as shown in Figure 4. The GPC turns out to be 0.081, 0.085, 0.094, and 0.142 nm at 250, 200, 150, and 100 °C, respectively (as plotted in Figure 5). It can be seen that the GPC of ZrO₂

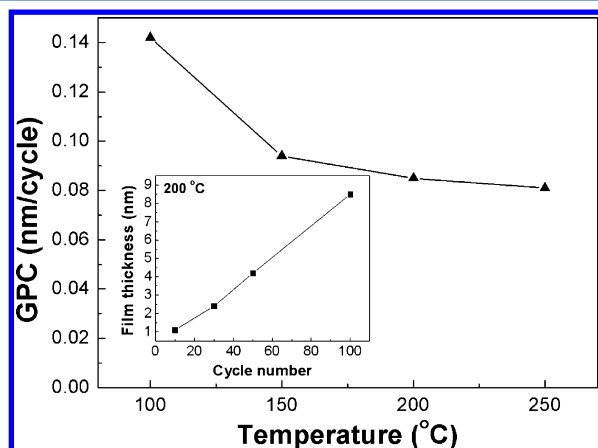


Figure 5. GPC of ALD-ZrO₂ on NCNTs as a function of deposition temperature (inset shows the thickness of ZrO₂ thin film deposited at 200 °C as a function of ALD cycle number).

stays almost the same (around 0.085 nm) from 250 to 150 °C. One can also find that the GPC of ZrO₂ at 100 °C (0.142 nm) is apparently higher than those at the other temperatures.

3.1.2. Growth Process of ALD-ZrO₂. The morphological evolution of ALD-ZrO₂ with ALD cycle was explored by SEM and HRTEM on the ZrO₂-NCNTs prepared at 200 °C and

presented in Figure 6. Comparing Figure 6a with b, it is obvious that the surface of NCNTs is coated with many nanoparticles after only five ALD cycles. With the increase of ALD cycles, these nanoparticles start to coalesce (Figure 6c) and eventually close into a uniform thin film after 30 cycles (Figure 6d). Further increasing ALD cycles leads to a thicker thin film with its uniformity maintained as shown in Figure 6e and Figure 3c. The morphological development of ALD-ZrO₂ was confirmed by HRTEM in Figure 6f–i. SEM observation on the ZrO₂-NCNTs prepared at 250, 150, and 100 °C indicates the similar growth process of ALD-ZrO₂ (Figures SI-4–6 of the Supporting Information). This phenomenon implies that the growth of ALD-ZrO₂ on NCNTs follows an island-growth mode at the very early stage and a layer-by-layer growth mode afterward.

HRTEM images of the ZrO₂-NCNTs prepared at 200 °C after different ALD cycles also disclose the crystalline development of ALD-ZrO₂ with ALD cycles as displayed in Figure 6f–i. Before 10 cycles, the ALD-ZrO₂ exhibits the amorphous state as seen in Figure 6f, g. After 30 cycles, the ALD-ZrO₂ thin film is still dominated by the amorphous phase in the matrix of which some crystalline tetragonal ZrO₂ nanoparticles (diameter around 1.5 nm) can be found (Figure 6h). With increasing ALD cycles, these crystalline ZrO₂ nanoparticles grow into bigger sizes, while the amorphous ZrO₂ thin film becomes thicker as shown in Figure 6i and Figure 3d. Thus, at 200 °C, the growth of amorphous ZrO₂ continues during the whole ALD process, while nucleation and growth of crystalline ZrO₂ start in the matrix of amorphous ZrO₂ at the intermediate stage. The thicknesses of ZrO₂ thin films after different ALD cycles at 200 °C are measured in Figure 6g–i and are plotted as a function of ALD cycle number (see the inset in Figure 5). In Figure 5, it can be clearly seen that the film thickness of ALD-ZrO₂ shows an almost linear relationship with ALD cycles indicating the self-limiting growth of ALD-ZrO₂ on NCNTs.

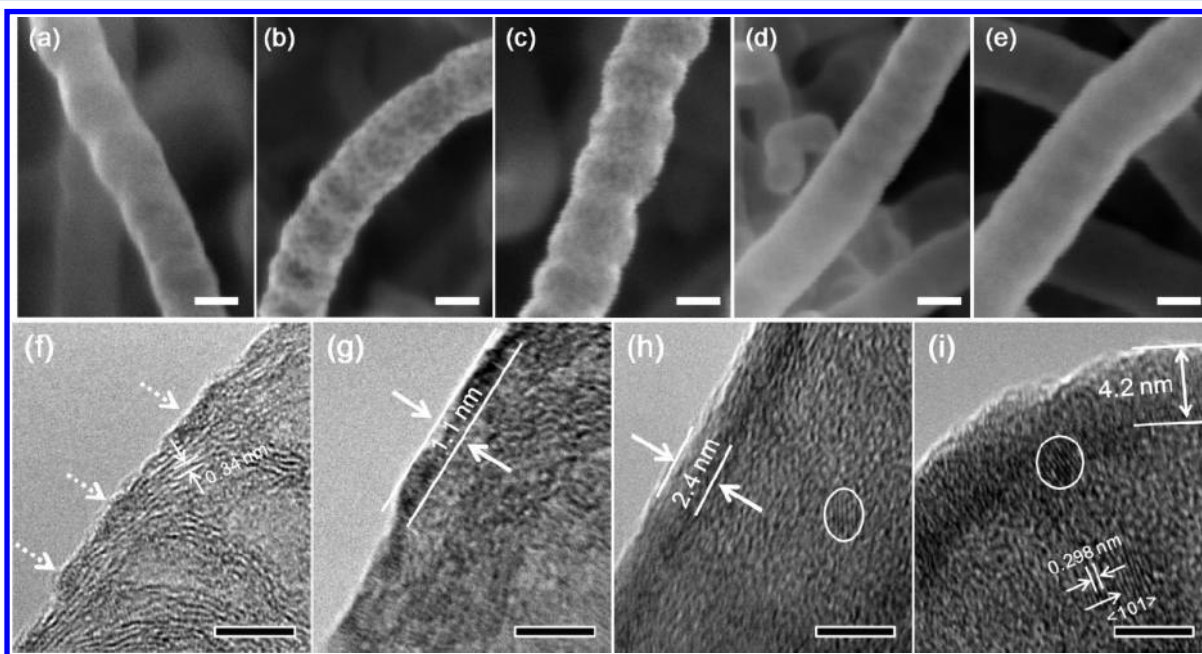


Figure 6. SEM images (a–e) of NCNTs without ZrO₂ coating (a) and with ZrO₂ coated at 200 °C after (b) 5 cycles, (c) 10 cycles, (d) 30 cycles, and (e) 50 cycles. HRTEM images (f–i) of NCNTs with ZrO₂ coated at 200 °C after (f) 5 cycles, (g) 10 cycles, (h) 30 cycles, and (i) 50 cycles. The scale bar in a–e and f–i represents 20 and 5 nm, respectively.

3.2. Discussion. From the results in section 3.1, one can easily see that ALD is distinguished as an innovative approach to synthesize ZrO_2 -NCNT nanocomposites in a well-controlled manner. The deposited ZrO_2 thin films not only have highly tunable crystallinity from amorphous to crystalline but also have precisely controlled thickness at the atomic level. The first feature is mainly ascribed to temperature dependence of ALD- ZrO_2 , whereas the second one results from the self-terminating nature of the ALD process. To better understand the characteristics of ALD- ZrO_2 , it is essentially important to clarify the influence of ALD process parameters, that is, the temperatures, substrates, and precursors,³⁶ on the growth process, the GPC, and the crystallinity of ALD- ZrO_2 on NCNTs.

As disclosed in section 3.1.2, the growth of ALD- ZrO_2 on NCNTs follows an island-growth mode at the very early stage and a layer-by-layer growth mode after coalescence of these islands into a thin film in a temperature range of 100–250 °C. Interestingly, island growth of ALD- ZrO_2 was also previously observed on the substrate of hydrogen-terminated silicon using ZrCl_4 and H_2O as precursors.^{50–52} The reason for this undesired ALD process was attributed to the lack of functional OH adsorption sites on the hydrogen-passivated surfaces, and the island growth of ZrO_2 started most likely at reactive defect sites of the substrate.⁵⁰ Another study reported that ZnO nanoparticles could be grown on single-walled carbon nanotubes (SWCNTs) by ALD because of the sparse amount of defective sites on SWCNTs.⁵³ Thus, the NCNT substrate in our case is believed to play a crucial role in determining the special growth process of ALD- ZrO_2 . As well-known, NCNTs are rich in surface defects induced by nitrogen doping.⁴³ These N-induced defects make the surface of NCNTs more reactive than that of CNTs and are thereby suitable for the direct growth of metal nanoparticles or nanowires on it.^{54,55} In our previous work, NCNTs were also employed as substrates for ALD- SnO_2 , and it was found that the surface defect sites, especially induced by pyridine-like N and graphite-like N, were preferable sites for the nucleation of ALD- SnO_2 .²⁹ Therefore, in this work, it is reasonable to believe that N-induced defect sites at the surface of NCNTs are responsible for the island growth of ALD- ZrO_2 at the very early stage. During the first cycle, $\text{Zr}(\text{NMe}_2)_4$ would chemically bond with these N-induced defect sites, and then introduced H_2O would react with the chemisorbed $\text{Zr}(\text{NMe}_2)_4$ via eq 2 generating –OH group terminated surface.³⁸ The following ALD cycles would happen preferably on the existing ZrO_2 surface via eq 1 and eq 2 sequentially leading to the island growth of ALD- ZrO_2 on NCNTs (see Figure 6b, f). With a further increase of ALD cycles, these ALD- ZrO_2 islands would grow in both vertical and lateral directions and finally would coalesce into a film (Figure 6c, d, g, h). From this point on, the deposition of ZrO_2 would occur on the film following a layer-by-layer growth mode (Figure 6e, i and Figure 3c, d). The thickness of ZrO_2 thin film can be simply but accurately controlled by the number of ALD cycles (see Figure 5). In addition, it was demonstrated that chemically bonded N in NCNTs was thermally stable up to 800 °C,⁵⁶ and thus, the N-induced defects on NCNTs in our case could be considered to remain unaffected by the temperature change from 100 to 250 °C. Moreover, theoretical calculation⁵⁷ showed that for $\text{Zr}(\text{NMe}_2)_4$, scission of metal–ligand bonds was more feasible than scission of N–C bonds, and experiment study³⁸ also indicated that the reaction of $\text{Zr}(\text{NMe}_2)_4$ and H_2O in ALD would follow eqs 1 and 2 in the temperature range of

100–250 °C. Therefore, in our case, it can be considered that the temperature change does not affect the substrate and the reaction mechanism of precursors. At all deposition temperatures, ALD- ZrO_2 followed a similar growth process, that is, island growth mode at the very early stage and layer-by-layer growth mode after the close of these islands into a thin film as presented in Figure 6 and Figures SI-4–6 of the Supporting Information.

GPC is an important factor to measure the growth of ALD materials. In this work, the GPC of ALD- ZrO_2 experienced an increase with decreasing temperature (see Figure 5). In particular, the GPC of ALD- ZrO_2 at 100 °C (0.142 nm) is obviously higher than those at the other temperatures (around 0.085 nm). Earlier studies have shown that the temperature could affect the GPC of ALD materials by having an effect on the number and types of reactive sites on the substrates and the preferred reaction mechanisms.³⁶ As discussed above, the temperature change from 100–250 °C seemed not to affect the reaction mechanism of $\text{Zr}(\text{NMe}_2)_4$ and H_2O in the ALD process.^{38,57} However, temperature does have an influence on the –OH groups, which were reactive sites for the ALD process and which were generated via eq 1. Many previous studies^{58–60} have indicated that the number and types of hydroxyl groups were temperature-dependent, and high temperature could lead to dehydroxylation. During ALD- ZrO_2 , the dehydroxylation of hydroxyl groups was described as follows:⁵⁹



Undoubtedly, this dehydroxylation would reduce the number of –OH groups and thereby would lead to a lower GPC at higher temperatures. Besides hydroxyl groups, physisorbed $\text{Zr}(\text{NMe}_2)_4$ and H_2O are probably accountable for the higher GPC at 100 °C. Ritala and Leskelä⁶¹ have shown that even at 500 °C, the desorption of water from the hydroxyl-terminated surface could be slow enough, and long purge periods were needed. Hausmann et al.³⁸ have proved that it took a much longer time to purge all surface-physisorbed $\text{Zr}(\text{NMe}_2)_4$ and H_2O at lower temperatures. Therefore, given the same purge time in our case, there would be more surface-physisorbed $\text{Zr}(\text{NMe}_2)_4$ and H_2O at lower temperatures, which would in return contribute to the growth of ZrO_2 . Surprisingly, the ZrO_2 thin film at lower temperatures still maintained its uniformity as shown in Figure 3 and Figure 4. A prolonged purge time (60 s) for both precursors did not obviously affect the thickness of ZrO_2 thin film (Figure SI-3 of the Supporting Information). Probably, a longer purge time than 60s is required in order to avoid the surface-physisorbed precursors, but it will inevitably increase the preparation time of ALD- ZrO_2 .

Besides growth mode and GPC, it is of great interest to explain the temperature dependence of the crystallinity of ALD- ZrO_2 . In section 3.1.1, one can find that the deposition temperature is the only parameter that distinguishes the four samples in this work. Apparently, it plays a crucial role in determining the crystallinity of ALD- ZrO_2 . A similar trend of crystallinity as a function of temperature was also previously reported in ALD-grown ZrO_2 ,^{38,62,63} TiO_2 ,^{28,64} HfO_2 ,⁶⁵ and SnO_2 .^{29,30} It was demonstrated that the temperature had strong effects on surface mobility of absorbed species,^{64,66} reaction mechanisms,^{29,30,63} and surface reactive sites^{29,63} thereby influencing the crystallinity of ALD-grown materials. High temperatures could enhance the surface mobility of absorbed species and could promote the ordering of the structure with minimum energy thus leading to the growth of crystallites.^{64,66}

Meng and co-workers^{29,30} prepared phase-controlled ALD-SnO₂ using SnCl₄ and H₂O as precursors and proposed that the change of reaction mechanism from ligand exchange and chlorination with increasing temperatures was responsible for the phase transition from amorphous to crystalline. In addition, Scarel et al.⁶³ suggested that the reaction mechanism between –OH species and ZrCl₄ could be changed by the decreased density of –OH species with increasing temperatures thus affecting the crystallinity of deposited ZrO₂. In our case, a higher temperature could help the mobilization of absorbed species and could enable the Zr and O ions to occupy the positions corresponding to the lowest free energy of the crystal⁶⁴ resulting in the crystalline phase of ALD-ZrO₂. XRD (Figure 2a) and HRTEM (Figure 4) results indicated that the ZrO₂ was preferentially oriented in the [101] direction, which seems to have the lowest free energy. Until now, there was no evidence showing that the reaction mechanism between Zr(NMe₂)₄ and H₂O is temperature-dependent in the temperature range we employed as discussed previously. Nonetheless, the increase of temperature can modify the surface reactive sites via the dehydroxylation process described in eq 3 leading to reduced hydroxyl groups at the surface. This might be a reason accountable for the increased crystallinity of ALD-ZrO₂ with elevating temperatures. Unfortunately, there is to date little knowledge about the effect of decreased hydroxyl groups on the reaction mechanism and the crystallinity of ALD-ZrO₂ using Zr(NMe₂)₄ and H₂O as precursors, and further investigations are needed. Another potential reason for ZrO₂ being amorphous at lower temperatures is the residual dimethylamido ligand in the film, which could possibly prevent the crystallization of ZrO₂. From the above discussion, one can clearly see the critical effect of temperature on the crystallinity of ZrO₂ at a given ALD cycle. On the other hand, at a given temperature, the crystallinity of ZrO₂ would be mainly related to the film thickness, and more crystalline ZrO₂ could be found in the thicker film as disclosed in Figure 6. This phenomenon was also observed in previous studies and could be explained as follows.^{39,67} At a given temperature, the nucleation events of crystalline ZrO₂ were distributed randomly over the surface of the substrate during each ALD cycle. The increase of ALD cycles could lead to the nucleation of more crystalline ZrO₂ nuclei in the thicker film. Once crystalline ZrO₂ nuclei formed, the following ALD cycle would contribute further mass to the nuclei resulting in the growth of crystalline ZrO₂. Therefore, the thicker film induced by more ALD cycles contained more crystalline ZrO₂ than the thinner film did. In this work, no more than 100 ALD cycles of ZrO₂ were used. A further increase of ALD cycles could lead to the change of ZrO₂ in its crystallinity (amorphous or crystalline),^{33,67} its phase (tetragonal, cubic, or monoclinic),⁶⁷ or even its surface roughness.³³

Figure 7 presents a schematic diagram to summarize the crystallite and morphological developments of ALD-ZrO₂ at temperatures between 100 and 250 °C. ZrO₂ exhibits only amorphous phase at 100 °C, whereas it exhibits only crystalline phase at 250 °C. At intermediate temperature (150–200 °C), the growth of amorphous ZrO₂ starts at the very beginning and continues during the whole process, while crystalline ZrO₂ nucleates and grows only during the intermediate process. Crystalline ZrO₂ was embedded in the matrix of amorphous ZrO₂ and did not affect the uniformity of the ZrO₂ thin film. At all temperatures, the growth of ALD-ZrO₂ follows an island-growth mode at the very early stage and a layer-by-layer growth mode after the coalescence of these islands into a film.

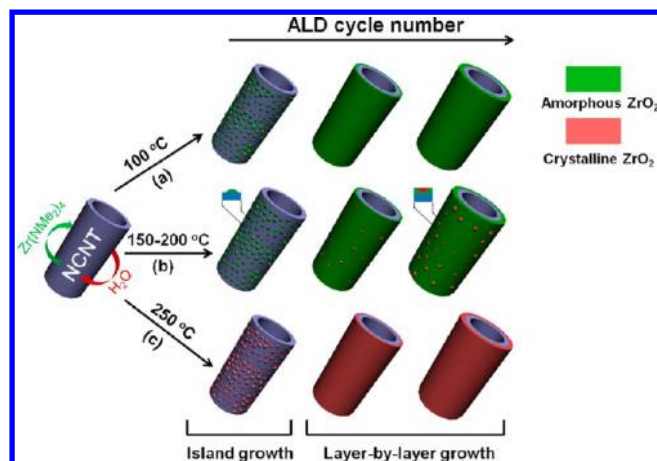


Figure 7. Schematic diagram for the growth mechanism of ALD-ZrO₂ on NCNTs at (a) 100 °C, (b) 150–200 °C, and (c) 250 °C.

4. CONCLUSIONS

In this work, ZrO₂-NCNT nanocomposites were successfully prepared by ALD at deposition temperatures from 100 to 250 °C. The results showed that the crystallinity of ZrO₂ thin film experienced a gradual decrease with the decrease of temperature. The deposition temperature of 250 °C resulted in pure crystalline ZrO₂, while 100 °C led to pure amorphous ZrO₂. Mixed phases of crystalline and amorphous ZrO₂ appeared in ZrO₂-NCNTs between 150 and 200 °C. The ZrO₂ thin film was very uniform and conformal. The GPC of ZrO₂ was 0.081, 0.085, 0.094, and 0.142 nm at 250, 200, 150, and 100 °C, respectively. At all deposition temperatures, the growth of ZrO₂ followed island-growth mode during the early stage and layer-by-layer growth mode after the coalescence of the islands into a film. It is expected that such ZrO₂-NCNT nanocomposites have great potential for various applications in fuel cells, batteries, electronics devices, and chemical sensors.

■ ASSOCIATED CONTENT

Supporting Information

SEM and TEM images of 50-cycle ZrO₂-NCNTs prepared at 100 and 200 °C; SEM images of ZrO₂-NCNTs prepared at 250, 150, and 100 °C with different ALD cycles. This material is available free of charge via the Internet at <http://pubs.acs.org>.

■ AUTHOR INFORMATION

Corresponding Author

*Tel: +1 519 661 2111 x87759; fax: +1 519 661 3020; e-mail: xsun@eng.uwo.ca (X.S.).

Notes

The authors declare no competing financial interest.

■ ACKNOWLEDGMENTS

This research was supported by General Motors of Canada, Natural Sciences and Engineering Research Council of Canada (NSERC), Canada Foundation for Innovation (CFI), Ontario Research Fund (ORF), Ontario Early Researcher Award (ERA), and University of Western Ontario. The authors also would like to thank Fred Pearson at McMaster University for his help on HRTEM.

■ REFERENCES

- (1) Iijima, S. *Nature* **1991**, *354*, 56–58.

- (2) Dresselhaus, M.; Dresselhaus, G.; Saito, R. *Carbon* **1995**, *33*, 883–891.
- (3) Okamoto, A.; Gunjishima, I.; Inoue, T.; Akoshima, M.; Miyagawa, H.; Nakano, T.; Baba, T.; Tanemura, M.; Oomi, G. *Carbon* **2011**, *49*, 294–298.
- (4) Baughman, R. H.; Zakhidov, A. A.; de Heer, W. A. *Science* **2002**, *297*, 787–792.
- (5) Gong, K.; Du, F.; Xia, Z.; Durstock, M.; Dai, L. *Science* **2009**, *323*, 760–764.
- (6) Guo, D. J.; Li, H. L. *Carbon* **2005**, *43*, 1259–1264.
- (7) Wang, Y. H.; Li, Y. N.; Zang, J. B.; Huang, H. *Nanotechnology* **2006**, *17*, 3817.
- (8) Morisada, Y.; Miyamoto, Y. *Mater. Sci. Eng., A* **2004**, *381*, 57–61.
- (9) Fu, L.; Liu, Z.; Liu, Y.; Han, B.; Wang, J.; Hu, P.; Cao, L.; Zhu, D. *Adv. Mater.* **2004**, *16*, 350–352.
- (10) Korneva, G.; Ye, H.; Gogotsi, Y.; Halverson, D.; Friedman, G.; Bradley, J.-C.; Kornev, K. G. *Nano Lett.* **2005**, *5*, 879–884.
- (11) Jitianu, A.; Cacciaguerra, T.; Benoit, R.; Delpeux, S.; Béguin, F.; Bonnamy, S. *Carbon* **2004**, *42*, 1147–1151.
- (12) Jiang, L.; Gao, L. *Mater. Chem. Phys.* **2005**, *91*, 313–316.
- (13) Liang, Y. X.; Chen, Y. J.; Wang, T. H. *Appl. Phys. Lett.* **2004**, *85*, 666–668.
- (14) Farmer, D. B.; Gordon, R. G. *Nano Lett.* **2006**, *6*, 699–703.
- (15) Piticescu, R. M.; Piticescu, R. R.; Taloi, D.; Badilita, V. *Nanotechnology* **2003**, *14*, 312.
- (16) Lu, J.; Zang, J. B.; Shan, S. X.; Huang, H.; Wang, Y. H. *Nano Lett.* **2008**, *8*, 4070–4074.
- (17) Luo, T. Y.; Liang, T. X.; Li, C. S. *Mater. Sci. Eng., A* **2004**, *366*, 206–209.
- (18) Liang, R.; Deng, M.; Cui, S.; Chen, H.; Qiu, J. *Mater. Res. Bull.* **2010**, *45*, 1855–1860.
- (19) Song, H.; Qiu, X.; Li, F. *Appl. Catal., A* **2009**, *364*, 1–7.
- (20) Guo, D.; Qiu, X.; Zhu, W.; Chen, L. *Appl. Catal., B* **2009**, *89*, 597–601.
- (21) Javey, A.; Kim, H.; Brink, M.; Wang, Q.; Ural, A.; Guo, J.; Mcintyre, P.; Mceuen, P.; Lundstrom, M.; Dai, H. *Nature* **2002**, *1*, 241–246.
- (22) Pal, K.; Kang, D. J.; Zhang, Z. X.; Kim, J. K. *Langmuir* **2010**, *26*, 3609–3614.
- (23) Sun, Z.; Zhang, X.; Na, N.; Liu, Z.; Han, B.; An, G. *J. Phys. Chem. B* **2006**, *110*, 13410–13414.
- (24) Shan, Y.; Gao, L. *Nanotechnology* **2005**, *16*, 625–630.
- (25) Lupo, F.; Kamalakaran, R.; Scheu, C.; Grobert, N.; Rühle, M. *Carbon* **2004**, *42*, 1995–1999.
- (26) Banerjee, S.; Hemraj-Benny, T.; Wong, S. S. *Adv. Mater.* **2005**, *17*, 17–29.
- (27) Lu, Y.; Bangsaruntip, S.; Wang, X.; Zhang, L.; Nishi, Y.; Dai, H. *J. Am. Chem. Soc.* **2006**, *128*, 3518–3519.
- (28) Meng, X.; Geng, D.; Liu, J.; Li, R.; Sun, X. *Nanotechnology* **2011**, *22*, 165602.
- (29) Meng, X.; Zhong, Y.; Sun, Y.; Banis, M. N.; Li, R.; Sun, X. *Carbon* **2011**, *49*, 1133–1144.
- (30) Meng, X.; Zhang, Y.; Sun, S.; Li, R.; Sun, X. *J. Mater. Chem.* **2011**, *21*, 12321–12330.
- (31) Meng, X.; Ionescu, M.; Banis, M.; Zhong, Y.; Liu, H.; Zhang, Y.; Sun, S.; Li, R.; Sun, X. *J. Nanopart. Res.* **2011**, *13*, 1207–1218.
- (32) Meng, X.; Geng, D.; Liu, J.; Banis, M.; Zhang, Y.; Li, R.; Sun, X. *J. Phys. Chem. C* **2010**, *114*, 18330–18337.
- (33) Chen, Y.; Wang, J.; Meng, X.; Zhong, Y.; Li, R.; Sun, X.; Ye, S.; Knights, S. *Int. J. Hydrogen Energy* **2011**, *36*, 11085–11092.
- (34) Li, X.; Meng, X.; Liu, J.; Geng, D.; Zhang, Y.; Banis, M.; Li, Y.; Li, R.; Sun, X.; Cai, M.; Verbrugge, M. *Adv. Funct. Mater.* **2012**, DOI: 10.1002/adfm.201101068.
- (35) George, S. M. *Chem. Rev.* **2010**, *110*, 111–131.
- (36) Puurunen, R. L. *J. Appl. Phys.* **2005**, *97*, 121301–121352.
- (37) Nam, W.-H.; Rhee, S.-W. *Chem. Vap. Deposition* **2004**, *10*, 201–205.
- (38) Hausmann, D. M.; Kim, E.; Becker, J.; Gordon, R. G. *Chem. Mater.* **2002**, *14*, 4350–4358.
- (39) Hausmann, D. M.; Gordon, R. G. *J. Cryst. Growth* **2003**, *249*, 251–261.
- (40) Becker, J. S.; Kim, E.; Gordon, R. G. *Chem. Mater.* **2004**, *16*, 3497–3501.
- (41) Liu, H.; Arato, D.; Li, R.; Zhang, Y.; Merel, P.; Sun, X. *Surf. Coat. Technol.* **2008**, *202*, 4114–4120.
- (42) Zhong, Y.; Jaidann, M.; Zhang, Y.; Zhang, G.; Liu, H.; Ionescu, M. I.; Li, R.; Sun, X.; Abou-Rachid, H.; Lussier, L.-S. *J. Phys. Chem. Solids* **2010**, *71*, 134–139.
- (43) Liu, H.; Zhang, Y.; Li, R.; Sun, X.; Désilets, S.; Abou-Rachid, H.; Jaidann, M.; Lussier, L.-S. *Carbon* **2010**, *48*, 1498–1507.
- (44) Hirata, T.; Asari, E.; Kitajima, M. *J. Solid State Chem.* **1994**, *110*, 201–207.
- (45) Keramidias, V. G.; White, W. B. *J. Am. Ceram. Soc.* **1974**, *57*, 22–24.
- (46) Ferrari, S.; Dekadjevi, D. T.; Spiga, S.; Tallarida, G.; Wiemer, C.; Fanciulli, M. *J. Non-Cryst. Solids* **2002**, *303*, 29–34.
- (47) Chen, L.; Mashimo, T.; Omurzak, E.; Okudera, H.; Iwamoto, C.; Yoshiasa, A. *J. Phys. Chem. C* **2011**, *115*, 9370–9375.
- (48) Pitcher, M. W.; Ushakov, S. V.; Navrotsky, A.; Woodfield, B. F.; Li, G.; Boerio-Goates, J.; Tissue, B. M. *J. Am. Ceram. Soc.* **2005**, *88*, 160–167.
- (49) Garvie, R. C. *J. Phys. Chem.* **1965**, *69*, 1238–1243.
- (50) Puurunen, R. L.; Vandervorst, W.; Besling, W. F. A.; Richard, O.; Bender, H.; Conard, T.; Zhao, C.; Delabie, A.; Caymax, M.; Gendt, S. D.; et al. *J. Appl. Phys.* **2004**, *86*, 4878–4889.
- (51) Copel, M.; Gribelyuk, M.; Gusev, E. *Appl. Phys. Lett.* **2000**, *76*, 436–438.
- (52) Besling, W. F. A.; Young, E.; Conard, T.; Zhao, C.; Carter, R.; Vandervorst, W.; Caymax, M.; De Gendt, S.; Heyns, M.; Maes, J.; et al. *J. Non-Cryst. Solid* **2002**, *303*, 123–133.
- (53) Min, Y. S.; Lee, I. H.; Lee, Y. H.; Hwang, C. S. *CrystEngComm* **2011**, *13*, 3451–3454.
- (54) Sun, C.-L.; Chen, L.-C.; Su, M.-C.; Hong, L.-S.; Chyan, O.; Hsu, C.-Y.; Chen, K.-H.; Chang, T.-F.; Chang, L. *Chem. Mater.* **2005**, *17*, 3749–3753.
- (55) Sun, S.; Zhang, G.; Zhong, Y.; Liu, H.; Li, R.; Zhou, X.; Sun, X. *Chem. Commun.* **2009**, *45*, 7048–7050.
- (56) Choi, H. C.; Bae, S. Y.; Jang, W.-S.; Park, J.; Song, H. J.; Shin, H.-J.; Jung, H.; Ahn, J.-P. *J. Phys. Chem. B* **2005**, *109*, 1683–1688.
- (57) Rodríguez-Reyes, J. C. F.; Teplyakov, A. V. *J. Appl. Phys.* **2008**, *104*, 084907.
- (58) Matero, R.; Rahtu, A.; Ritala, M.; Leskelä, M.; Sajavaara, T. *Thin Solid Films* **2000**, *368*, 1–7.
- (59) Cassir, M.; Goubin, F.; Bernay, C.; Vernoux, P.; Lincot, D. *Appl. Surf. Sci.* **2002**, *193*, 120–128.
- (60) Aarik, J.; Aidla, A.; Sammelselg, V.; Siimon, H.; Uustare, T. *J. Cryst. Growth* **1996**, *169*, 496–502.
- (61) Ritala, M.; Leskelä, M. *Appl. Surf. Sci.* **1994**, *75*, 333–340.
- (62) Kukli, K.; Ritala, M.; Asrik, J.; Uustare, T. *J. Appl. Phys.* **2002**, *92*, 1833–1840.
- (63) Scarel, G.; Ferrari, S.; Spiga, S.; Wiemer, C.; Tallarida, G.; Fanciulli, M. *J. Vac. Sci. Technol., A* **2003**, *21*, 1359–1365.
- (64) Aarik, J.; Aidla, A.; Uustare, T.; Sammelselg, V. *J. Cryst. Growth* **1995**, *148*, 268–275.
- (65) Ritala, M.; Leskelä, M.; Niinistö, L.; Prohaska, T.; Friedbacher, G.; Grasserbauer, M. *Thin Solid Films* **1994**, *250*, 72–80.
- (66) Goodman, C. H. L.; Pessa, M. V. *J. Appl. Phys.* **1986**, *60*, R65–R81.
- (67) Aarik, J.; Aidla, A.; Mändar, H.; Uustare, T.; Sammelselg, V. *Thin Solid Films* **2002**, *408*, 97–103.